MDPI

Article

Computational Inertial Microfluidics: Optimal Design for Particle Separation

Suvash C. Saha *, Isabella Francis and Tanya Nassir

School of Mechanical and Mechatronic Engineering, Faculty of Engineering and Information Technology, University of Technology Sydney, Ultimo, NSW 2007, Australia
* Correspondence: Suvash.Saha@uts.edu.au

Abstract: Following the emergence of many blood transfusion-associated diseases, novel passive cell separation technologies, such as microfluidic devices, are increasingly designed and optimized to separate red blood cells (RBCs) and white blood cells (WBCs) from whole blood. These systems allow for the rapid diagnosis of diseases without relying on complicated and expensive hematology instruments such as flow microscopes, coagulation analyzers, and cytometers. The inertia effect and the impact of intrinsic hydrodynamic forces, the Dean drag force (F_D), and the inertial lift force (F_L) on the migration of particles within curved and complex confined channels have been explored theoretically, computationally, and experimentally. This study aimed to optimize the dimensions of a microfluidic channel for fast particle propagation and separation. Several spiral geometries with different cross-sections were tested using computational fluid dynamics (CFD) to separate two particle types representing RBCs and WBCs. The chosen three geometries consist of a single inlet, two outlets, and three spiral turns, each having a different cross-sectional height (120, 135, and 150 μm). Particle separation was successfully achieved in the 135 μm-height microchannel, while other microchannels demonstrated mixed particle types at the outlets.

Keywords: computational inertial microfluidics; particle trajectory; particle separation; cell separation; red/white blood cells; microfluidics channel; cross-section

1. Introduction

Inertial microfluidics emerged from the discovery of inertial focusing [1–3] and has recently gained popularity as modern computational resources are providing easier access to various flow channel designs [4–6]. In addition, the high-volume sample processing, significant throughput rate, and broad accessibility of microfluidic chips [7] enable them to replace traditional cell isolation, fractionation, and purification methods [8,9]. Inertial microfluidics predicts cell trajectories and behavior based on channel geometry, natural hydrodynamic forces, and particle's intrinsic characteristics (diameter size, deformability, charge, and density) [10].

Numerous studies have employed a semi-analytical asymptotic analysis that included the two most fundamental forces in inertial studies: lift and drag forces exerted by Dean flows [11]. The early stages of this method compared the particle trajectory in confined channels against a free flow and found that particles experience more resistance in bounded areas near the walls. Asmolov et al. [12] developed the first efficient model to predict the inertial behavior of particles in confined microchannels, relating the lift force to the particle slip velocity at low Reynolds numbers (Re). The model also determined the number of particle equilibrium positions and their locations under different conditions. However, this semi-analytical method had many limitations regarding the particle Reynolds number, large particle sizes, complex channel geometries, and viscoelastic flows. Another followed method is the lattice Boltzmann method (LBM), a CFD approach initially introduced by McNamara and Zenetti [13] that successfully simulates fluid flows and transport processes.

This method illustrated that the fluid path is approximated by the discrete particle arrangements and their lattice collision. This process summarized the physical mechanism of particle behavior associated with the Reynolds number and the vortices within the channels. The LBM system is one of the few approaches that effectively explain inertial particle motion in Serpentine microchannels. In low Re, the particles have a closer proximity to the wall due to the increased lift force. In high Re, drag force (F_D) takes over, and the Dean flow vortex forces the particle out of the lift force flow and more towards the center of the Dean vortex [14]. In more recent studies, the LBM was used to solve the Navier–Stokes equations in 3D simulations. Such a method discretizes the velocity vectors and accounts for the particle-to-particle behavior [15]. Although this method exhibited some advantages over the previous technique, such as its accuracy and coupling mathematical ability, it had some limitations. First, due to the "dead" volume in spirals, it is difficult to apply the method's original form since it relies on a cubic lattice. Second, this method has many boundary conditions that need to be considered and optimized for different particles and geometries. Third, the performance of this method is inaccurate in pressure fields that cause an impact on the lift and drag forces. However, when such a method is combined and mastered with Palabos (parallel lattice Boltzmann solver) or MATLAB, advanced C or C++ libraries can establish parallel calculations, graphical interpretation, and model complex time-dependent geometries. For example, Kotsalos et al. [16] performed a relatively successful coupling between the finite element method (FEM) structural solver–LBM and the Palabos existing library. The study achieved an axial focus on the FEM-LBM solver for the deformability of RBCs and an immersive boundary condition method to account for the particle–fluid interaction. In addition, further suggestions and recommendations were made to include a collision model that allows for particle-to-particle interaction. However, the study only stretched into including the behavior of a single particle in the body of fluid. As stated previously, the behavior of a fluid depends on the inertial lift force, drag force, and shear force. These competing forces, along with the microchannel cross-sectional area and number of walls, affect the equilibrium of the particles [17]. For example, particles settle in a ring-shaped equilibrium position at a fixed distance from the center in a circular or oval channel. However, in a rectangular cross-sectional area of a straight channel, two possible equilibrium positions are located close to the walls [18]. In addition, Amini et al. [19] stressed that the particle size ratio to microchannel size and control over the length of the microchannel can determine the adequacy of the microfluidic system to inertially separate the particles and differentiate the equilibrium positions.

In a curved channel, the particles that reach an equilibrium between F_L and F_D tend to follow the inner wall curve and can therefore be targeted by the inner outlet. However, the particles with an unequal F_L-to-F_D ratio tend to migrate to the outer wall of the microchannel as observed and, therefore, can be targeted and collected via the outer outlet [20]. This notion will allow for the prediction of blood particle trajectories and assume that white blood cells (WBCs) will focus closer to the inner wall due to their larger size, and that the red blood cells (RBCs) will migrate closer to the center and or the outer wall depending on the geometric properties of the slant in the cross-sectional area. This would allow the collection of the cells using the two-outlet system, which was also validated by Nivedita and Papautsky [21].

In this study, the focus is on separating blood cells in the most optimal geometry. The cross-sectional area of the microchannel is optimized by changing the dimensions of the complex model to achieve fast and successful particle separation with constant flow and particle properties.

2. Methods

2.1. Optimal Design

Previously, several inertial microfluidics techniques were developed for cell sorting and dynamic fluid manipulation. However, to cater to the complexity of deformable bio-particles such as blood cells, a combination of sorting techniques and cross-sectional

area geometry must be integrated. Therefore, the development of cascaded systems that encompass multiple designs has gained popularity through the studies of Nam et al. [22] and Sonmez et al. [17]. The research in such papers created the base design case for the optimal spiral geometry to increase the efficiency of throughput and capturing ability. Jeon et al. [23] utilized a multidimensional double spiral (MDDS) that contained a rectangle cross-sectional area in the first spiral and a trapezoidal in the second spiral to achieve successful blood cell separation. The study concludes that separation performance can be altered by channel dimensions, reduction of particle–particle interaction, and the number of spiral loops. A further adapted version of a slanted spiral with three loops was implemented as the optimal design for the computational simulation to analyze particle behavior in confined channels.

A number of parameters were studied and optimized to reach final separation. The parameters crucial for data analysis include the capture rate, Reynolds number, aspect ratio, and geometric design manipulability [24,25]. The capture rate refers to the percentage of particles captured at each outlet, which evaluates the effectiveness of the outlet system model and ensures efficient functionality. The Reynolds number analysis is related to the fluid's volume flow rate and velocity at the inlet, which affects the particle behavior in the microchannel. The aspect ratio is the ratio between the height (h) and the width (w) of the channel, which is pre-defined in the design geometry.

A spiral geometry with a trapezoidal and rectangular cross-section was created using SOLIDWORKS 2020 and designed considering three ratios. First was the aspect ratio, where the stability of particle migration occurred at $h/w = 1/3$. Second was the confinement ratio λ where $\lambda = a/D_h$, with a being the particle diameter and D_h the hydraulic diameter. Third was the curvature ratio δ which determines the strength of the Dean vortex where $\delta = D_h/2r$ with r being the innermost radius of the channel curvature [26].

The optimal design (Figure 1a) having successful particle separation based on results produced by COMSOL Multiphysics 6.0, has an equal length and width of 1 cm, three spiral turns, one inlet, and two outlets. The cross-section (Figure 1b) consists of a 135 μm outer wall height, 100 μm inner wall height, and 500 μm total base width with a relaxed angular slant of 5.71. This design has an aspect ratio of $h/w = 0.27$ and a confinement ratio λ of 0.056 for WBCs and 0.028 for RBCs. For comparison purposes, another two models were tested for RBCs and WBCs particle separation. The height was changed to 120 μm in the first with an aspect ratio of 0.24, and to 150 μm in the second with an aspect ratio of 0.3.
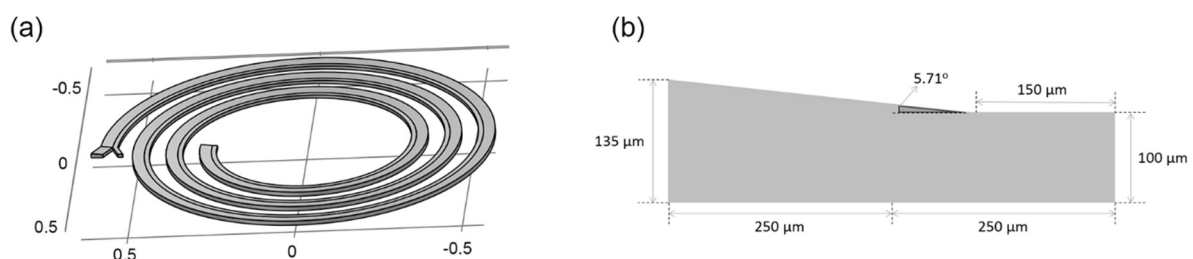
Figure 1. (**a**) Tilted top view of the spiral design with dimensions in cm. (**b**) Cross-sectional dimensions of the spiral geometry composed of a right-angled trapezoid and a rectangle.

2.2. Force Analysis

Within a confined spiral geometry, the generated inertia created a Dean vortex limited to the trapezoidal part of the cross-sectional area. Therefore, by increasing the strength of the Dean vortex, the particles travel along a narrower path and take a unique equilibrium position depending on the forces exerted by the carrier fluid. These forces include the Dean drag force [27], $\mathbf{F_D} = 3\pi U_D a$, where U_D is the Dean velocity and a is the particle diameter. The Dean velocity is a function of the Dean number (D_e) through the equation $U_D = 1.8 \times 10^{-4} De^{1.63}$, where the Dean number is a function of spiral geometry dimensions through the equation, $D_e = Re\sqrt{\frac{D_h}{2R_C}}$, with R_C being the radius of the spiral channel, D_h

being the hydraulic diameter proportional to the height (h), and the width (w) of the channel as $D_h = \frac{2hw}{(h+w)}$. Another force is the inertial lift force [28,29], which primarily impacts the location of larger particles and is quantified through the equation $F_L = \frac{2\rho(U_F)^2(a_c)^4}{D_h{}^2}$, with U_F being the mean velocity of the fluid. Two types of lift forces exist: the Saffman lift force and the wall-induced lift force. The Saffman lift force is applied to particles far from the wall of the specified geometry. In contrast, the wall-induced lift force accounts for the effects of nearby walls as particles move through pipes/channels, which is applicable for this case. The latter lift force uses a first-order correction to the velocity profile at the channel walls and a second-order correction at the surface of the particle in order to account for higher-order derivatives of the fluid velocity [30].

2.3. Meshing and Mesh Dependent Test

Five different mesh sizes ranging from extra coarse mesh to fine mesh with tetrahedral elements and near-wall boundary layers were generated by the physics-controlled meshing sequences inbuilt on COMSOL Multiphysics 6.0 [30] to ensure the accuracy of the results. The flow velocity at a line on the cross-section directly before the outlet (0.5 cm) was the output parameter for the mesh test. Figure 2c shows that the velocity magnitudes (m/s) of the different mesh sizes exhibit approximately equal values along the line of length 500 μm. An error percentage table (Figure 2d) demonstrated the percentage differences between the different meshes in comparison with the fine mesh, and Figure 2e reflects the mesh element size to differentiate between the selected meshes for the study. For this design, a coarse mesh (Figure 1a) with a 0.987% error was chosen to perform the simulation. The error term describes particle velocity convergence for a point velocity method or a bounding line at the pre-outlet stage. Mesh modification was achieved using two different methods that were embedded within COMSOL. Adaptive mesh refinement was chosen when conducting the final draft mesh progression. Adaptive mesh enables the software to calculate where the error is higher relative to the geometrical structure and then isolate the error section to be re-meshed in the specified area to re-solve for the physics specified. Figure 1b demonstrates a zoomed-in view of the tetrahedral elements comprising the chosen coarse mesh.

2.4. Numerical Methods

The Navier–Stokes equations for the conservation of mass and momentum for unsteady and incompressible flows were solved using a commercial finite element-based program, COMSOL Multiphysics 6.0. Due to the small diameter of the microchannel, relatively low velocities, and therefore the low Reynolds number (Re), the flow field was solved using the laminar flow [31] module. Within COMSOL, the laminar flow module contains the Dean force and the shear gradient lift force between particles and walls. Given that the motion in the laminar domain can be identified as a sparse flow with small particle mass, volume, and density, the drag force feature was required. For low fluid Re numbers, the Stokes's law, which allows for wall correction, was used to solve for the drag force. The conservation of mass (1) and momentum Equation (2) are the following:

$$\rho\nabla.u=0 \tag{1}$$

$$\rho(u.\nabla u)=\nabla.[-p+\mu(\nabla u+(\nabla u)^T)]+F \tag{2}$$

Here, ρ is the density, u is the velocity field, p is the pressure, μ is the dynamic viscosity, and F is the total volume force. Despite the fact that blood is a non-Newtonian fluid, in most clinical applications including inertial microfluidics systems, the blood sample is diluted 50 to 100 times. Therefore, water is considered a suitable fluid to replace the cells' carrier as the plasma in the simulation with a density of $\rho = 1000$ kg/m^3 and a dynamic viscosity of $\mu = 0.001$ Pa·s. Blood particles WBC and RBC were adjusted to reflect the true particle density and dynamic viscosity under the particle tracing model. For the simulation of the solid particles, the particle tracing module allowed for the computation of particles as

background fluids. The equation used to describe the motion of the particles is computed using the following equation of motion:

$$\frac{d}{dt}(m_p v) = F_D + F_G + F_{ext} \tag{3}$$

Here, m_p represents the mass (kg) of the particles, v is the particle velocity (m/s), F_D is the integrated Drag force (N), F_G is the force (N) due to gravity, and F_{ext} represents other external forces (N) that act on the particle. Particle motion can be driven by drag, gravity, electric, magnetic, lift, and acoustophoretic forces. In this case, the drag and lift forces were the only two forces acting on the particles. The inbuilt module options allowed for allocations of particle release specifications based on the release time or mass flow rate. The particle release time was selected enabling each particle to be treated as the instantaneous position of one or more particles for the accurate modeling of fluid–particle interaction. White blood cells and red blood cells were released at time $t = 0$ s. In addition, the particle diameter was crucial in reflecting particle behavior as it determines the aspect ratio affecting the flow in the confined microchannel. Two different types of particles were considered: The particle representing a white blood cell (WBC) with a diameter of $d = 12$ μm and density $\rho = 1050$ kg/m^3, and the particle representing a red blood cell (RBC) with the same density with a diameter of $d = 6$ μm. A projected plane grid was selected for the particle node release where a total of 120 particles (100 RBC and 20 WBC) were uniformly distributed on a plane grid tangential to the inlet.
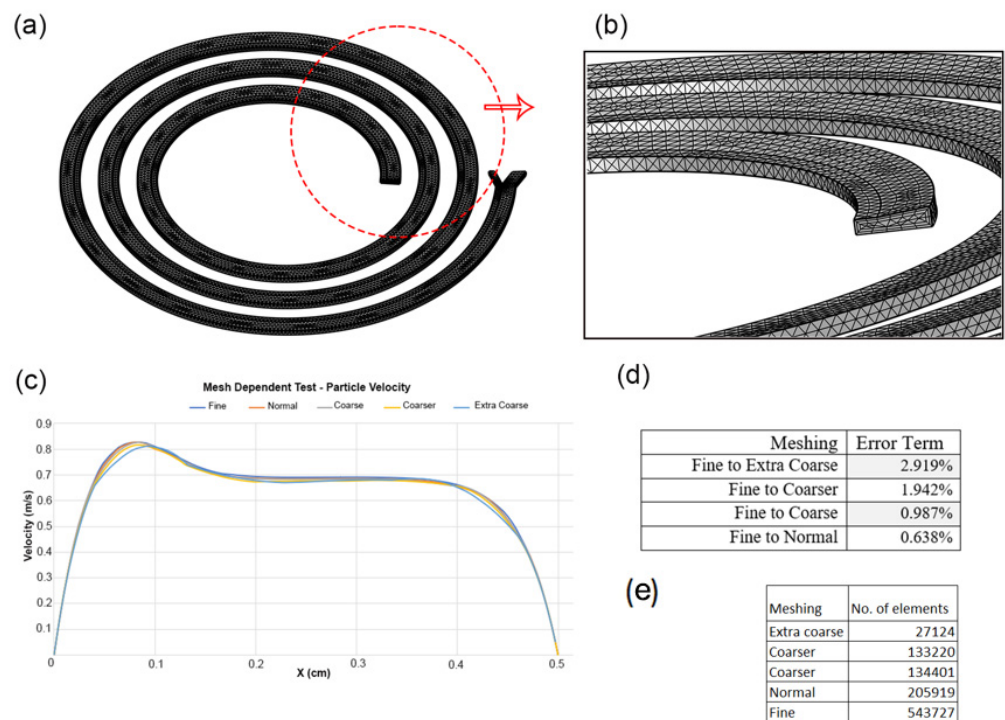
Figure 2. (a) Top view of the meshed spiral geometry. (b) Zoomed-in view of the tetrahedral elements. (c) Mesh-dependent test based on the velocity (m/s) at a line located just before the outlet. (d) Mesh errors in comparison to the fine mesh. (e) Number of tetrahedral elements in the mesh-dependent analysis against meshing type.

For one microchannel geometry, five simulations were performed, each with a different inlet velocity value (0.25, 0.35, 0.45, 0.50, and 0.55 m/s), to find the optimum inlet velocity for successful particle separation. After choosing the most appropriate inlet velocity, two other similar simulations were performed for different microchannel models with different cross-sectional heights. For each simulation, a second-order pressure discretization was

set to account for the shear gradient force applied to the particles. A zero-pressure outlet, no-slip wall boundary condition, and particle bouncing condition were imposed on the walls. The Saffman law for lift forces is dedicated to axial particle behavior with a mid-channel focus, away from walls. In contrast, the wall-induced law for lift forces portrays a specialized formulation to consider the effects of the walls as particles travel through the confined space. In the rectangular cross-section shape of this design, the particles tend to reach equilibrium and travel closer to walls, and therefore, the wall-induced lift force law was selected. The first was placed at the side walls (inner and outer walls of the spiral), and the second was at the top and bottom walls of the enclosed channel.

3. Results and Discussion

3.1. Velocity and Dean Vortex

Inertial particle focusing was most successful in simulations with higher inlet velocities (0.5 and 0.55 m/s). Due to the increase in the Reynolds number, a more substantial Dean flow led to a clearer distinction between the heavy (WBCs) and light particles (RBCs). In contrast, particles at 0.25 and 0.35 m/s inlet velocities followed a spaced-out equilibrium and settled closer to the mid-section of the channel, thus mixing both particle types and failing to achieve particle separation.

In the confined channel, the velocity profile perpendicular to the direction of fluid flow exhibited the same airfoil shape in every spiral turn and at any location, with velocity magnitudes ranging from 0 m/s at the walls (no-slipping condition) to a maximum velocity of 0.55 m/s towards the left of the trapezoidal cross-section (Figure 3a,b). The velocity magnitudes were higher in the trapezoidal cross-section (outer wall) in comparison to the rectangular cross-section (inner wall). The flow accelerated near the outer wall as the maximum velocity (0.9 m/s) exceeded the initial inlet constant velocity (0.55 m/s). Similar results were obtained for other microfluidics numerical and experimental simulations, with near-zero velocities near the wall and a maximum velocity of around 0.9 m/s [32,33]. The imbalance of force between the higher velocity flow near the outer wall and the lower velocity flow near the inner wall generated counter-rotating vortices. A velocity arrow plot at a vertically-cut slice (Figure 3c) illustrated the Dean vortex (secondary flow) formation in the microfluidic channel.
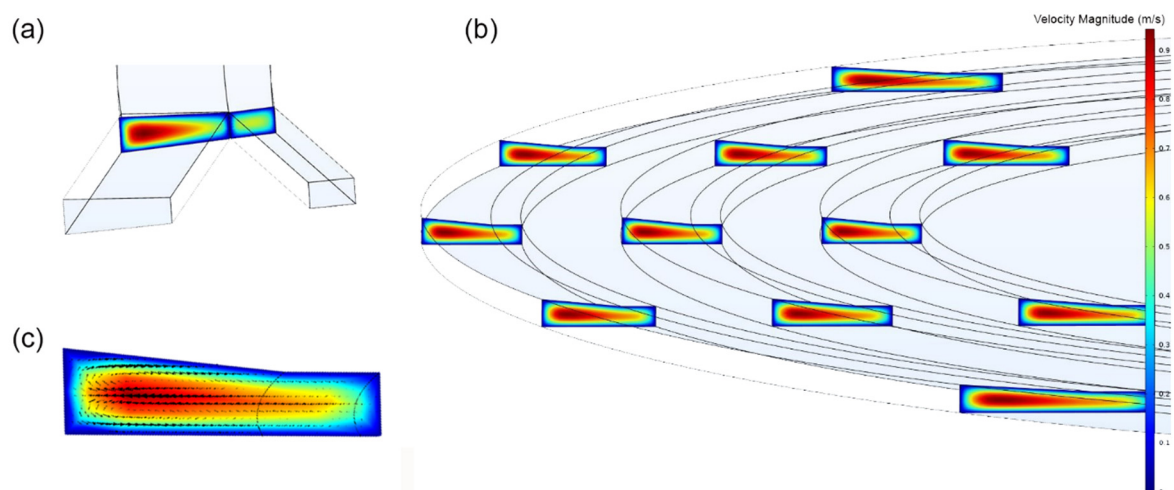

Figure 3. (**a**) Velocity contours normal to the fluid flow at the two outlets and (**b**) at different selected horizontal planes of the spiral geometry. (**c**) Normal velocity vectors at a random vertically cut slice.

3.2. Optimum Particle Separation

A transient simulation for displaying the trajectories of blood particles representing WBCs (red color) and RBCs (blue color) was performed for an optimum time of 3 seconds with a time step size of 0.001 s. Between the four different microchannel models, the 135 μm outer wall height demonstrated the best particle separation.

Figure 4a displays the spiral with red-colored WBCs of a 12 μm diameter and blue-colored RBCs of a 6 μm diameter. The results show that for the designed geometry with the specific cross-sectional values, the three turns were sufficient for successful particle separation (Figure 4b). The particle trajectory was formulated based on the Dean vortex and the effect of drag and lift forces. The Dean vortices and the accompanied forces shifted the larger WBC particles towards the inner wall curve until they attained equilibrium between the F_L and F_D forces and exited from the rectangular outlet. However, the smaller particles with an unequal F_L and F_D migrated to the outer wall of the microchannel. Similarly, the effect of the secondary flow on the RBCs and WBCs particle separation has been demonstrated in other experimental and numerical studies [14,34], where the different sized particles obtain different final equilibrium positions. For this study, from the initially released 100 RBCs, 99 successfully separated from the WBCs at the outlets, with only one RBC exiting with the 20 WBCs (Figure 4c).
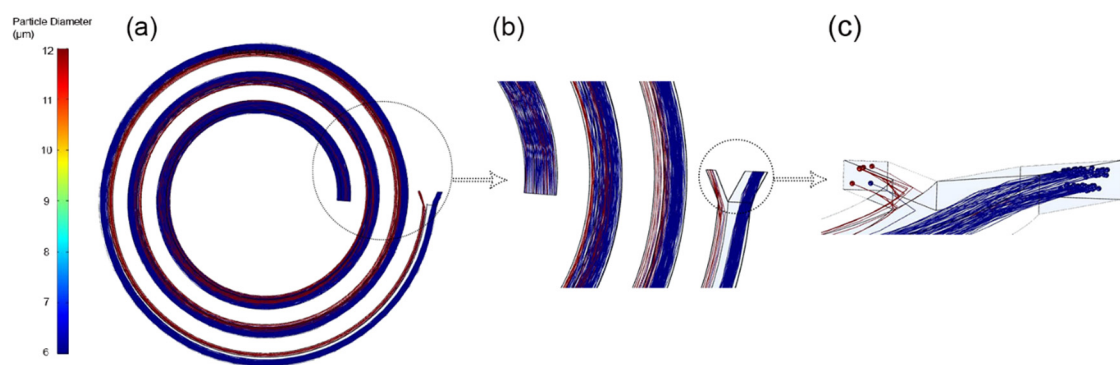

Figure 4. (**a**) Particle diameter differentiation inside the 135 μm height spiral; (**b**) zoomed-in view on particle trajectory reaching the outlets; (**c**) zoomed-in view on the two outlets with clear particle separation.

As this spiral geometry provides fast and accurate particle separation, it can be used in many biomedical and medical applications such as cancer diagnostics, chemical and biological analyses, and drug discovery for cell sorting and separation.

3.3. Validation of Design

Two additional simulations with different wall heights were performed. Similar boundary conditions, flow, and particle properties were utilized to simulate the flow and particle separation in 120 and 150 μm outer wall heights of the microchannel. Less successful particle separation was observed for both simulations in comparison to the 135 μm wall height. Figure 5 shows noticeable RBCs and WBCs mixing in the rectangular outlet of the 120 μm outer wall height microchannel. Out of the 100 RBCs initially released from the inlet, 10 of them separated from the rest and led to a mild unsuccessful particle separation.

Figure 6 shows the particle separation for the 150 μm outer wall height microchannel, where seven vertically-cut slices (Figure 6a) were used to observe the shift in RBCs and WBCs during each spiral turn (Figure 6b). Figure 6a demonstrates seven Poincaré slices in 2D space, including the inlet surface and a plane directly before the two outlets. Figure 6b displays a zoomed-in view of the Poincaré slices on the left side of the microchannel. Initially, both particle types were randomly distributed along the cross-section of the channel inlet. Then, the Dean vortex pushed each particle type in opposite directions, where most red particles (WBCs) traveled along with the Dean vortex by gradually shifting from right to left (inner wall) as they progressed from the second turn to the third. The blue ones (RBCs) exhibited an opposite motion from left to right (outer wall). For this 150 μm outer wall height microchannel, 20 RBC particles out of the initial 100 were mixed with the WBCs in the rectangular outlet.
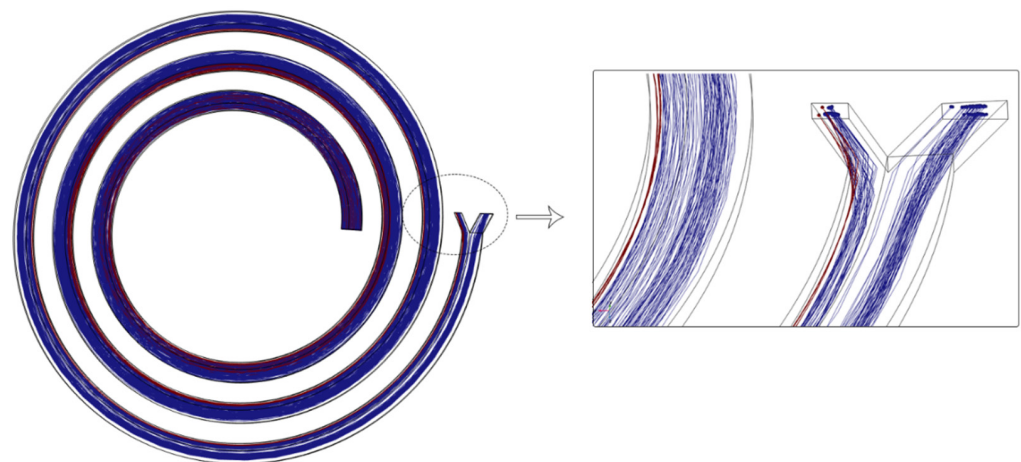
Figure 5. Particle separation inside the 120 μm height spiral with a zoomed-in view on the two outlets showing mixed particle types.
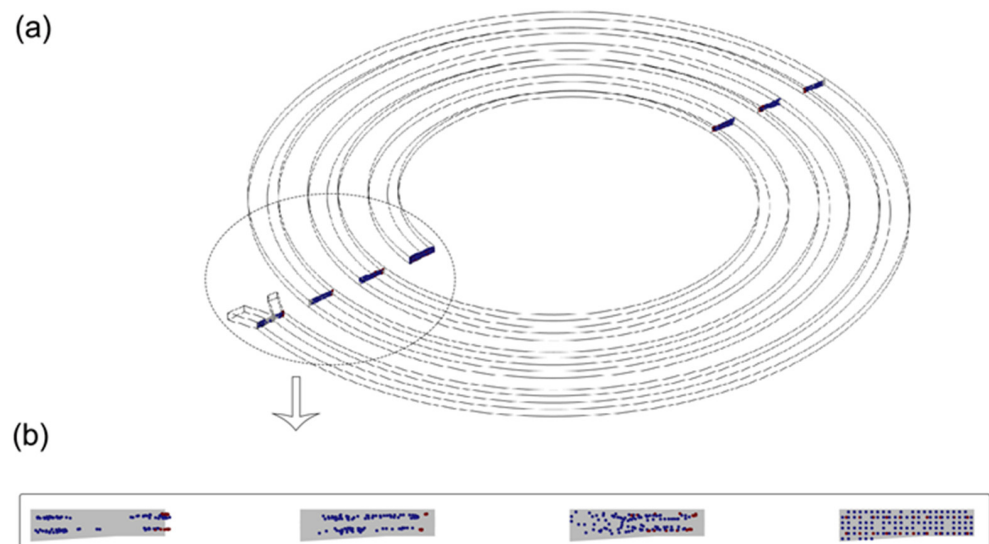
Figure 6. (**a**) Seven vertically-cut planes in the 150 μm height spiral. (**b**) Zoomed-in view on the left side of the microchannel showing scattered particles at each spiral turn.

3.4. COMSOL Simulation Optimisation

The COMSOL simulation was optimized throughout the numerical simulation to reflect the results to be expected during experimentation studies. Additional nodes were introduced to account for particle interaction with the fluid, where the fluid–particle interaction interface was used in conjunction with particle tracing to reflect the drag effect caused by the fluid and imposed on the WBC and RBC. A no-slipping boundary condition was introduced to the walls of the channels, and geometry was smoothed to ensure that the edges would not result in singularities. In modeling for fluid flow, the bounding equations were not only coupled, but they established a nonlinear relationship specific to inertia terms. Further optimization of the model was completed in an effort to re-evaluate the finite element method (FEM) and the use of discretisation to eliminate numerical diffusion. COMSOL requires streamlining diffusion to be active when higher-order discretization such as the P2 + P2 and P3 + P3 is allocated [35]. COMSOL's fluid flow interface calculates the cell Re number for all non-zero values in the process of discretization, typically shown as Rec = $\rho |u| h/(2\mu)$, whereby h is the element length. This is directly related to the stability of the numerical solution of discretization. As the Re of the cell grows, the risk for diffusion increases [36]. This model adopted P2 + P2 high-order discretization to reduce numerical diffusion.

4. Conclusion and Limitations

This study developed a complex design that successfully separated RBCs in the outer wall outlet and WBCs in the inner wall outlet using the effect of a Dean vortex. The cross-sectional outer wall height was varied to achieve the most successful particle separation. Comparing the three simulations, the particle separation percentage error was the highest (20%) in the 150 μm outer wall height, followed by 10% in the 120 μm outer wall height, and 1% in the 135 μm outer wall height. Limitations of this study include considering a two-way coupling between the fluid and the particles but ignoring the two-way coupling of particle–particle interaction, simulating a relatively small number of particles, and assuming spherical non-deforming red blood cells. We did not consider the elastic collisions of red cells with the wall, and this model is limited to dilute suspension. Future studies will address these limitations and consider different microchannel geometries with different cross-sections for 100% particle separation accuracy. Another consideration will be the successful separation of more than two particle types and diameters.

Nomenclature

Re	Reynolds number
w	width of the channel
h	height of the channel
RBC	red blood cell
WBC	white blood cell
De	Dean number
U_D	Dean velocity (m/s)
D_h	hydraulic diameter (m)
P	pressure (Pa)
$\boldsymbol{F_D}$	drag force (N)
$\boldsymbol{F_L}$	lift force (N)
D	diameter (μm)
t	time (s)
Symbols	
δ	curvature ratio
λ	confinement ratio
$\boldsymbol{\rho}$	density (kg/m^3)
$\boldsymbol{\mu}$	dynamic viscosity (kg/m·s)

References

1. Segre, G.; Silberberg, A. Radial particle displacements in Poiseuille flow of suspensions. *Nature* **1961**, *189*, 209–210. [CrossRef]
2. Zhou, J.; Papautsky, I. Fundamentals of inertial focusing in microchannels. *Lab Chip* **2013**, *13*, 1121–1132. [CrossRef] [PubMed]
3. Martel, J.M.; Toner, M. Inertial focusing in microfluidics. *Annu. Rev. Biomed. Eng.* **2014**, *16*, 371. [CrossRef]
4. Tan, Y.-C.; Fisher, J.S.; Lee, A.I.; Cristini, V.; Lee, A.P. Design of microfluidic channel geometries for the control of droplet volume, chemical concentration, and sorting. *Lab Chip* **2004**, *4*, 292–298. [CrossRef] [PubMed]

5. Braff, W.A.; Bazant, M.Z.; Buie, C.R. Inertial effects on the generation of co-laminar flows. *J. Fluid Mech.* **2015**, *767*, 85–94. [CrossRef]
6. Bazaz, S.R.; Mashhadian, A.; Ehsani, A.; Saha, S.C.; Krüger, T.; Warkiani, M.E. Computational inertial microfluidics: A review. *Lab A Chip* **2020**, *20*, 1023–1048. [CrossRef]
7. Sajeesh, P.; Sen, A.K. Particle separation and sorting in microfluidic devices: A review. *Microfluid. Nanofluid.* **2014**, *17*, 1–52. [CrossRef]
8. Di Carlo, D. Inertial microfluidics. *Lab A Chip* **2009**, *9*, 3038–3046. [CrossRef]
9. Nasiri, R.; Shamloo, A.; Ahadian, S.; Amirifar, L.; Akbari, J.; Goudie, M.J.; Lee, K.; Ashammakhi, N.; Dokmeci, M.R.; Di Carlo, D. Microfluidic-based approaches in targeted cell/particle separation based on physical properties: Fundamentals and applications. *Small* **2020**, *16*, 2000171. [CrossRef]
10. Shields IV, C.W.; Reyes, C.D.; López, G.P. Microfluidic cell sorting: A review of the advances in the separation of cells from debulking to rare cell isolation. *Lab Chip* **2015**, *15*, 1230–1249. [CrossRef]
11. Tripathi, E.; Patowari, P.K.; Pati, S. Numerical investigation of mixing performance in spiral micromixers based on Dean flows and chaotic advection. *Chem. Eng. Processing-Process Intensif.* **2021**, *169*, 108609. [CrossRef]
12. Asmolov, E.S.; Dubov, A.L.; Nizkaya, T.V.; Harting, J.; Vinogradova, O.I. Inertial focusing of finite-size particles in microchannels. *J. Fluid Mech.* **2018**, *840*, 613–630. [CrossRef]
13. McNamara, G.R.; Zanetti, G. Use of the Boltzmann equation to simulate lattice-gas automata. *Phys. Rev. Lett.* **1988**, *61*, 2332. [CrossRef] [PubMed]
14. Jiang, D.; Tang, W.; Xiang, N.; Ni, Z. Numerical simulation of particle focusing in a symmetrical serpentine microchannel. *RSC Adv.* **2016**, *6*, 57647–57657. [CrossRef]
15. Schaaf, C.; Stark, H. Particle pairs and trains in inertial microfluidics. *Eur. Phys. J. E* **2020**, *43*, 1–13. [CrossRef]
16. Kotsalos, C.; Latt, J.; Chopard, B. Bridging the computational gap between mesoscopic and continuum modeling of red blood cells for fully resolved blood flow. *J. Comput. Phys.* **2019**, *398*, 108905. [CrossRef]
17. Sonmez, U.; Jaber, S.; Trabzon, L. Super-enhanced particle focusing in a novel microchannel geometry using inertial microfluidics. *J. Micromech. Microeng.* **2017**, *27*, 065003. [CrossRef]
18. Gou, Y.; Jia, Y.; Wang, P.; Sun, C. Progress of inertial microfluidics in principle and application. *Sensors* **2018**, *18*, 1762. [CrossRef]
19. Amini, H.; Lee, W.; Di Carlo, D. Inertial microfluidic physics. *Lab Chip* **2014**, *14*, 2739–2761. [CrossRef]
20. Hou, H.W.; Warkiani, M.E.; Khoo, B.L.; Li, Z.R.; Soo, R.A.; Tan, D.S.-W.; Lim, W.-T.; Han, J.; Bhagat, A.A.S.; Lim, C.T. Isolation and retrieval of circulating tumor cells using centrifugal forces. *Sci. Rep.* **2013**, *3*, 1259. [CrossRef]
21. Nivedita, N.; Papautsky, I. Continuous separation of blood cells in spiral microfluidic devices. *Biomicrofluidics* **2013**, *7*, 054101. [CrossRef] [PubMed]
22. Nam, J.; Namgung, B.; Lim, C.T.; Bae, J.-E.; Leo, H.L.; Cho, K.S.; Kim, S. Microfluidic device for sheathless particle focusing and separation using a viscoelastic fluid. *J. Chromatogr. A* **2015**, *1406*, 244–250. [CrossRef] [PubMed]
23. Jeon, H.; A Khan, Z.; Barakat, E.; Park, S. Label-free electrochemical microfluidic chip for the antimicrobial susceptibility testing. *Antibiotics* **2020**, *9*, 348. [CrossRef] [PubMed]
24. Weddemann, A.; Wittbracht, F.; Auge, A.; Hütten, A. Positioning system for particles in microfluidic structures. *Microfluid. Nanofluid.* **2009**, *7*, 849–855. [CrossRef]
25. Mogi, K.; Fujii, T. A microfluidic device for stepwise size-based capturing of suspended particles. *J. Micromech. Microeng.* **2010**, *20*, 055015. [CrossRef]
26. Martel, J.M.; Toner, M. Particle focusing in curved microfluidic channels. *Sci. Rep.* **2013**, *3*, 3340. [CrossRef]
27. Bhagat, A.A.S.; Kuntaegowdanahalli, S.S.; Papautsky, I. Continuous particle separation in spiral microchannels using dean flows and differential migration. *Lab Chip* **2008**, *8*, 1906–1914. [CrossRef]
28. Park, J.-S.; Song, S.-H.; Jung, H.-I. Continuous focusing of microparticles using inertial lift force and vorticity via multi-orifice microfluidic channels. *Lab Chip* **2009**, *9*, 939–948. [CrossRef]
29. Nieuwstadt, H.A.; Seda, R.; Li, D.S.; Fowlkes, J.B.; Bull, J.L. Microfluidic particle sorting utilizing inertial lift force. *Biomed. Microdevices* **2011**, *13*, 97–105. [CrossRef]
30. Guide, I. *Comsol Multiphysics*; Version 5.6, COMSOL AB; COMSOL Inc.: Stockholm, Sweden, 1998; pp. 204–208.
31. Lagerstrom, P.A. *Laminar Flow Theory*; Princeton University Press: Princeton, NY, USA, 1996.
32. Mashhadian, A.; Shamloo, A. Inertial microfluidics: A method for fast prediction of focusing pattern of particles in the cross section of the channel. *Anal. Chim. Acta* **2019**, *1083*, 137–149. [CrossRef]
33. Palumbo, J.; Navi, M.; Tsai, S.S.; Spelt, J.K.; Papini, M. Inertial particle separation in helical channels: A calibrated numerical analysis. *AIP Adv.* **2020**, *10*, 125101. [CrossRef]
34. Ni, C.; Jiang, D. Three-dimensional numerical simulation of particle focusing and separation in viscoelastic fluids. *Micromachines* **2020**, *11*, 908. [CrossRef] [PubMed]
35. Multiphysics, C. *Introduction to Comsol Multiphysics®*; COMSOL Multiphysics; COMSOL Inc.: Stockholm, Sweden, 1998; Volume 9, p. 32.
36. Kuzmin, D.; Mierka, O.; Turek, S. On the Implementation of the k-[Epsilon] Turbulence Model in Incompressible Flow Solvers Based on a Finite Element Discretization. *Int. J. Comput. Sci. Math.* **2007**, *1*, 193–206. [CrossRef]